Protein Engineering, Design and Selection, 2026, **39**, gzag031
https://doi.org/10.1093/protein/gzag031
Published: 22 October 2026
Original Article

Engineering a hyperstable synthetic miniprotein for B7-H3 targeting

Hannah K. Windsor[1], Nicholas C. Ulen[1], Claudia Beaudry[2], Benjamin J. Hackel[1,2,*]

[1]Department of Chemical Engineering and Materials Science, University of Minnesota – Twin Cities, Minneapolis, MN 55455, United States
[2]Department of Biomedical Engineering, University of Minnesota – Twin Cities, Minneapolis, MN 55455, United States
*Corresponding author. Department of Chemical Engineering and Materials Science, University of Minnesota – Twin Cities, Minneapolis, MN 55455, United States. E-mail: hackel@umn.edu
Editor: Arne Skerra.

Abstract

Small protein ligands, such as miniproteins, have the potential to provide the efficient physiological transport and rapid clearance required for radioligand therapy. Yet, binders require single-digit nanomolar affinity for potent targeting and high stability for radiolabeling and physiological integrity. High-affinity and stable single-domain miniproteins are also modular candidates for multispecific applications in cell engagers and avid constructs. Previous work demonstrated computationally designed 40-amino acid $\beta\alpha\beta\beta$ miniproteins as effective scaffolds for ligand discovery. Herein, to yield the desired single-digit nanomolar affinity for B7-H3, an important immune regulator and cell surface antigen upregulated in numerous tumors, we used structural modeling to guide experimental evolution of the lead molecule. We performed constrained diversification at six sites on a β-sheet, structurally distinct from the originally engineered α-helical paratope, as well as nine sites within the α-helix, and sorted for strong binding to B7-H3 *via* yeast display and flow cytometry with detergent-solubilized cell lysate. Top variants discovered from this campaign yielded affinities of 8.4 and 11 nM, with the most performant variant, named βm.1, resulting in 1.2 ± 0.2 nM affinity. βm.1 had four β-sheet mutations relative to parental and $T_{m,app} \geq 91°C$, with reversible unfolding. The lead variant, βm.1, putatively engages B7-H3 at the same domain I epitope as the parental lead but with improved engagement *via* a T27F mutation and three homologous mutations. βm.1 is a hyperstable, high-affinity miniprotein B7-H3 binder with compelling potential for radioligand therapy and multispecific applications.

Keywords B7-H3, miniprotein, ligand, directed evolution, affinity maturation

Introduction

Radioligand therapy serves as a powerful method to selectively deliver ionizing radiation to a tumor while limiting background toxicity through molecular targeting to a cancer biomarker (Sgouros *et al.* 2020). The approvals of Pluvicto (Sartor *et al.* 2021) and Lutathera (Strosberg *et al.* 2017) demonstrate the efficacy of radioligand therapies in the clinic. However, these treatments are limited to prostate and neuroendocrine cancers, and significant work generating radioligands to additional targets is crucial to expanding the breadth of cancers able to be treated (Minati *et al.* 2020; Passaro *et al.* 2024). Radioligands comprise a high-affinity, specific binder to the therapeutic target, an α- or β-emitting radioisotope (Ninatti *et al.* 2025; To *et al.* 2025), and a linker connecting the two. The potency of radioligand therapy benefits from highly selective delivery including (1) exquisitely target-specific binding to avoid non-tumor delivery, (2) single-digit nanomolar or better binding affinity to retain activity at the tumor (Adams *et al.* 2001; Schmidt and Wittrup, 2009; Zahnd *et al.* 2010; Okarvi and Jammaz, 2012; Orcutt *et al.* 2012; Thurber and Dane Wittrup, 2012; Tolmachev *et al.* 2012), (3) efficient tumor uptake *via* blood vessel extravasation and tissue penetration (Thurber and Wittrup, 2012), (4) rapid clearance of unbound agent to reduce toxicity, and (5) high thermal and chemical stability to enable radiolabeling and maintain integrity in the physiological environment. These transport requirements – for clearance, extravasation, and penetration – are best achieved by low molecular weight (Schmidt and Wittrup, 2009; Wittrup *et al.* 2012), while the requirements of strong, selective binding are effectively achieved by engineered proteins with appreciable paratope area (Chen *et al.* 2013a). Engineering molecules to combine the requisite binding, transport, and biophysical robustness is a distinct challenge that has hampered the broader development of radioligand therapy.

Proteins offer several beneficial attributes to serve as scaffolds for radioligand therapies (Liu *et al.* 2021). Proteins are efficiently engineered *via* display technologies (Smith and Petrenko, 1997; Gai and Wittrup, 2007; Cherf and Cochran, 2015; Jaroszewicz

Received: 26 February 2026. **Revised:** 20 September 2026. **Accepted:** 3 October 2026
© The Author(s) 2026. Published by Oxford University Press.
This is an Open Access article distributed under the terms of the Creative Commons Attribution-NonCommercial License (https://creativecommons.org/licenses/by-nc/4.0/), which permits non-commercial re-use, distribution, and reproduction in any medium, provided the original work is properly cited. For commercial re-use, please contact reprints@oup.com for reprints and translation rights for reprints. All other permissions can be obtained through our RightsLink service via the Permissions link on the article page on our site—for further information please contact journals.permissions@oup.com.

et al. 2022; He and Taussig, 2007) for highly specific, high-affinity binding and are suggested to reach FDA approvals faster than small molecules (Gurevich and Gurevich, 2014; Kintzing *et al.* 2016; Senior, 2023). While antibodies are the dominant protein scaffold in the biologics space, and known for high affinity interactions, their large size (∼150 kDa) and Fc domains hinder tumor penetration and result in slow pharmacokinetics (Thurber and Dane Wittrup, 2012; Zhang *et al.* 2023). Additionally, antibodies may experience poor developability characteristics such as low recombinant expression (Zhang *et al.* 2022), modest thermal stability (Zhang *et al.* 2023; Condado-Morales *et al.* 2024), aggregation (Lowe *et al.* 2011; Dudgeon *et al.* 2012), and immunogenicity (Harding *et al.* 2010), all of which limit manufacturing and/or therapeutic success. At the other end of the size spectrum, small molecules and peptides provide superior transport properties, yet they are more challenging to engineer to the specificity and affinity requisite for strong performance (Chen *et al.* 2013a). Moreover, unconstrained peptides are inherently susceptible to proteolysis (McGregor, 2008), although cyclization (Walensky and Bird, 2014; Chow *et al.* 2019) or alternative modulation (Werle and Bernkop-Schnürch, 2006; Lucana *et al.* 2021; Höppner *et al.* 2025) can impart significant stability. Miniproteins, at the lower size limit of proteins with folded tertiary structure (∼4–8 kDa) (Baker *et al.* 2017), can merge the benefits of both molecular classes with small size for advantageous transport, (Schmidt and Wittrup, 2009; Thurber and Wittrup, 2012) modifiable surface area, and structural constraint to enable high-affinity, selective binding. For example, Gp2 (Kruziki *et al.* 2015), affibodies(Frejd and Kim, 2017; Vasilescu *et al.* 2025), cysteine knots (Reinwarth *et al.* 2012) and more (Gurevich and Gurevich, 2014; Baker *et al.* 2017) have all been engineered to bind various protein targets.

Developability varies across different miniproteins (Ożga and Berlicki, 2022). We have recently advanced computationally designed miniproteins as ligand scaffolds. Rocklin, Baker, and team *de novo* designed hyperstable sequences for multiple protein folds with thermal and chemical stability beyond natural proteins (Rocklin *et al.* 2017). In a pair of manuscripts, our lab demonstrated the ability to leverage several of these designs, with particular diversified paratopes, as frameworks for evolvable ligand scaffolds with single-digit nanomolar affinity and robust developability (Blanchard *et al.* 2023; McConnell *et al.* 2023). The 40-amino acid $\beta\alpha\beta\beta$ topology (three β-strands with an α-helix after the first strand; see Fig. 1) served as a scaffold for potent binders to seven different targets with high target selectively and maintained high thermal stability (Blanchard *et al.* 2023).

Of the many binders evolved from $\beta\alpha\beta\beta$ scaffolds, one campaign targeted B7-H3 (also known as CD276) (Blanchard *et al.* 2023). B7-H3 is overexpressed in various cancers such as lung (Yonesaka *et al.* 2018), prostate (Shi *et al.* 2022), ovarian(Zang *et al.* 2010; Lutz *et al.* 2014), breast(Arigami *et al.* 2010), and more (Zhou and Jin, 2021; Miller *et al.* 2024). The B7 family of proteins are cell surface receptors known for the regulatory roles they play within the immune system and cancer progression (Ceeraz *et al.* 2013). B7 proteins stimulate or inhibit lymphocytes serving as crucial immune checkpoints. B7-H3 is pro-tumorigenic as it enables cancer cells to evade the immune system and therefore associated with poor patient prognosis (Zhou and Jin, 2021; Zafar *et al.* 2025). The breadth of cancer types, and poor outcomes associated with B7-H3 make it a desirable target for expansion of radioligand therapy.

Our prior work discovered lead B7-H3 binding $\beta\alpha\beta\beta$ variants which stemmed from various frameworks and paratopes, of which variant 1 (v1) was derived from framework 2 (EHEE_rd2_0008 from Rocklin *et al.*(Rocklin *et al.* 2017)) and diversified within the α-helix paratope (Fig. 1A). Subsequent characterization of v1 measured the equilibrium dissociation constant (K_d) for soluble extracellular domain of B7-H3 at 11 ± 5 nM and an apparent midpoint of thermal denaturation ($T_{m,app}$) of $\geq$88°C. Additionally, v1 maintained high specificity, preferentially binding to B7-H3 over other cancer biomarkers, prostate-specific membrane antigen (PSMA) and cluster of differentiation 22 (CD22) (Blanchard *et al.* 2023). As an initial lead, v1 satisfies the thermal stability and high specificity requirements to serve as a B7-H3 targeting radioligand, but requires affinity maturation to reach the desired single-digit nanomolar potency for cellular B7-H3 for future *in vivo* applications.

We performed directed evolution from v1 to engineer a variant with the desired increase in affinity, while maintaining the previously achieved high selectivity and stability. We synthesized and sorted a pair of structurally informed yeast libraries, one diversifying parental v1 in the original α-helix paratope and a second diversifying a β-sheet computationally predicted to engage B7-H3 in v1. The libraries underwent iterative selections with magnetic beads and flow cytometry to enrich binders to cellular B7-H3. We identified a variant with 1.2 nM affinity for cellular B7-H3, increased stability ($T_{m,\,app} \geq 91$°C) with reversible unfolding, and maintained specific binding to B7-H3.

Results

Library design and generation

We sought to improve the affinity of v1 by directed evolution of the binding interface. While mutations distal to an active site can also aid binding (Wang *et al.* 2006; Osuna, 2021), mutations within the active site have more frequent and more substantial impact (Gerton *et al.* 1998; Ucisik and Hammes-Schiffer, 2017). To identify the potential binding paratope, we modeled the interface between v1 and the extracellular domain (ECD) of human B7-H3 using AlphaFold 3 (AF3) (Abramson *et al.* 2024) (Fig. 1). While noting that model confidence was limited (ipTM = 0.53), the putative binding interface of v1 on B7-H3 demonstrates engagement of the originally diversified paratope (Fig. 1B, red α-helix) as expected. Yet, there were also six residues within the final two β-strands on the miniprotein within 4 Å of B7-H3 (Fig. 1B, blue). Therefore, we decided to assess evolution of the nine original α-helix sites in addition to the six β-strand sites. To enable broad chemical diversity while achieving deep sampling, we assembled and sorted two libraries, called the α library and the β library for their respective secondary structures. Within the α library, six of nine sites (9, 10, 13, 14, 17, 20) were diversified for a large breadth of chemical functionality due to their probable engagement with B7-H3 residues. The remaining three residues (11, 18, 21) were given a narrow diversification, as they were part of the original paratope, but not within 4 Å of B7-H3 in the AF3 model (Supplementary Fig. 1). For these residues, diversification focused on maintaining similar physiochemical properties to the parental residue (Fig. 1C). In the β library, all positions were diversified for physicochemical breadth (Fig. 1D) while limiting excessive diversity to prevent destabilization. Sites 25, 27 and 28 received the same diversification, encompassing select aromatic, aliphatic, polar, and charged

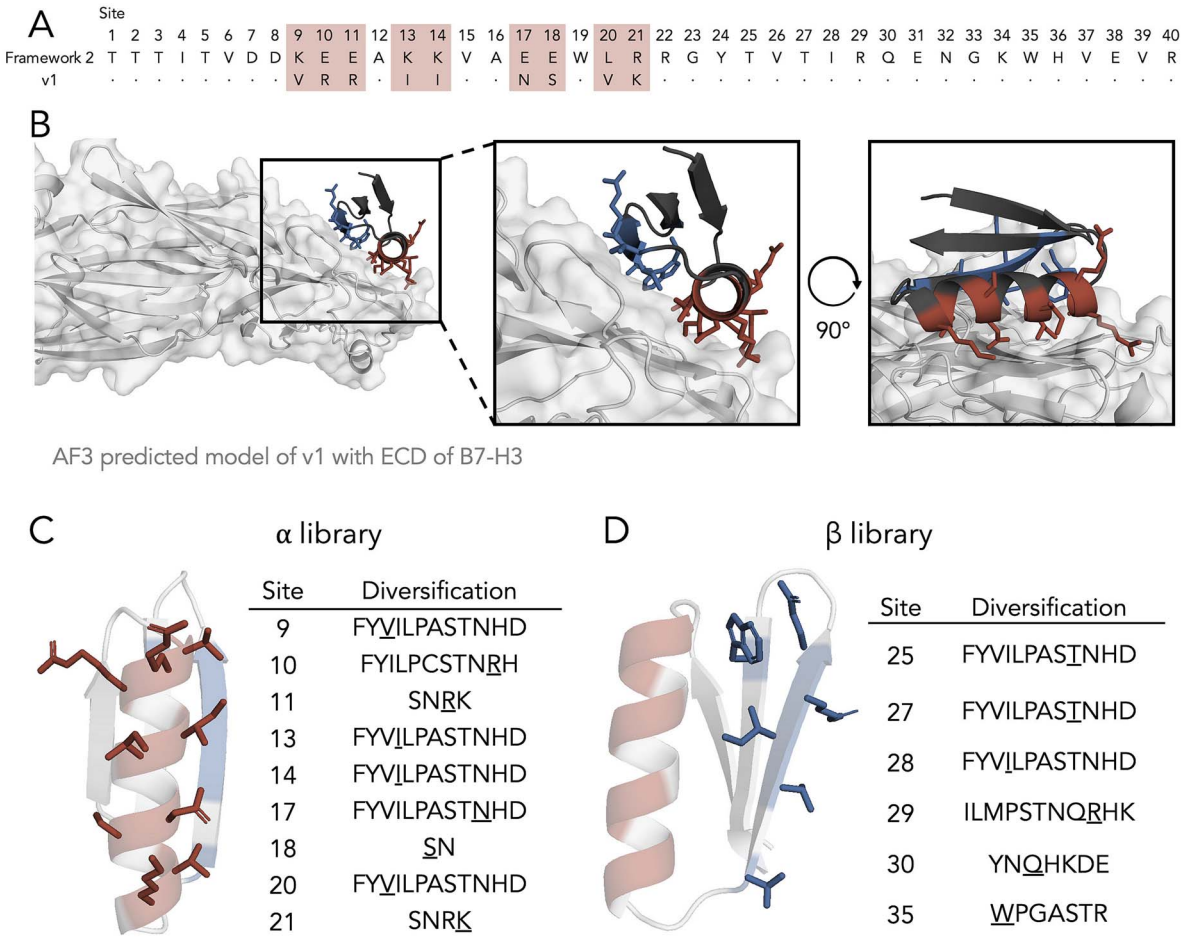


Figure 1 v1 library design. (A) Sequence alignment of v1 with its parental scaffold framework 2. Red shaded boxes indicate original diversification sites from the parental $\beta\alpha\beta\beta$ framework 2. (B) The bound complex structure of v1 (dark grey) and human B7-H3 extracellular domain (amino acids 1–456, light grey) was predicted in AlphaFold3 (AF3). The original diversification sites on the α-helix are shown in red. Six sites within the last two β-strands that reside within 4 Å of B7-H3 are shown in blue. pTM = 0.41. ipTM = 0.53 (C,D) Library designs for the α paratope (C) and β paratope (D) are shown with underlines indicating the parental v1 amino acid residue. pTM = 0.41.

residues. Site 29 had a similar extent of diversity but with slightly more hydrophilic options because of its moderate engagement with B7-H3 and increased solvent exposure (solvent-accessible surface area [SASA] (Fraczkiewicz and Braun, 1998) in the proposed complex: 99%, Supplemental Fig. 1). Site 35 minimized the number of residue options because of its potential engagement with the scaffold core (SASA in unbound miniprotein: 24%; Supplemental Fig. 1). Finally, site 30 received a large bias towards polar and charged residues to encourage hydrogen-bond interactions on the nearby loop of B7-H3 (Fig. 1B, Supplemental Fig. 1). This design yielded theoretical diversities of 9.6×10^7 and 9.3×10^5 for the α and β libraries, respectively. Each library was assembled *via* overlap PCR of degenerate oligonucleotides (Supplemental Table 1) and subsequent homologous recombination with the pCT-80 vector suitable for yeast display with an extended polypeptide linker (Stern *et al.* 2016). The α library yielded a diversity of 4.3×10^8 transformants (4.5× coverage) while the β library resulted in 6.1×10^8 transformants (660× coverage). Sequencing of the α and β libraries demonstrates matching to the intended design, with 0.3% and 0.7% average absolute deviation at diversified sites for the α and β libraries, respectively (Supplemental Figs. 2 and 3).

Library selection

Yeast displaying the miniprotein libraries were separately sorted to enrich the highest affinity B7-H3 binders. Two rounds of monovalent magnetic bead activated cell sorting (MACS) were completed followed by fluorescence-activated cell sorting (FACS). Some cell surface targets are not effectively mimicked by recombinant soluble extracellular domain formats, because of alternative folding, oligomerization, post-translational modification, or epitope accessibility in the distinctive formats (Stern *et al.* 2019; Ribeiro *et al.* 2024). Thus, we utilized detergent-solubilized cell lysate of B7-H3-expressing cells as the target form herein. To identify strong, selective binding to the physiological form of this transmembrane cell surface target, both libraries were depleted of non-specific binders to streptavidin and IgG followed by subsequent enrichment of binders to 0.5 nM detergent-solubilized lysate from MS1 cells overexpressing B7-H3 ($MS1^{B7\text{-}H3}$; Supplemental Table 2) (Lutz *et al.* 2014). Monovalent MACS entails incubating yeast-displaying variants with monovalent biotinylated B7-H3 lysate followed by removal of unbound biotinylated B7-H3. Target-bound yeast were then captured on streptavidin-coated magnetic beads. A second round of streptavidin and

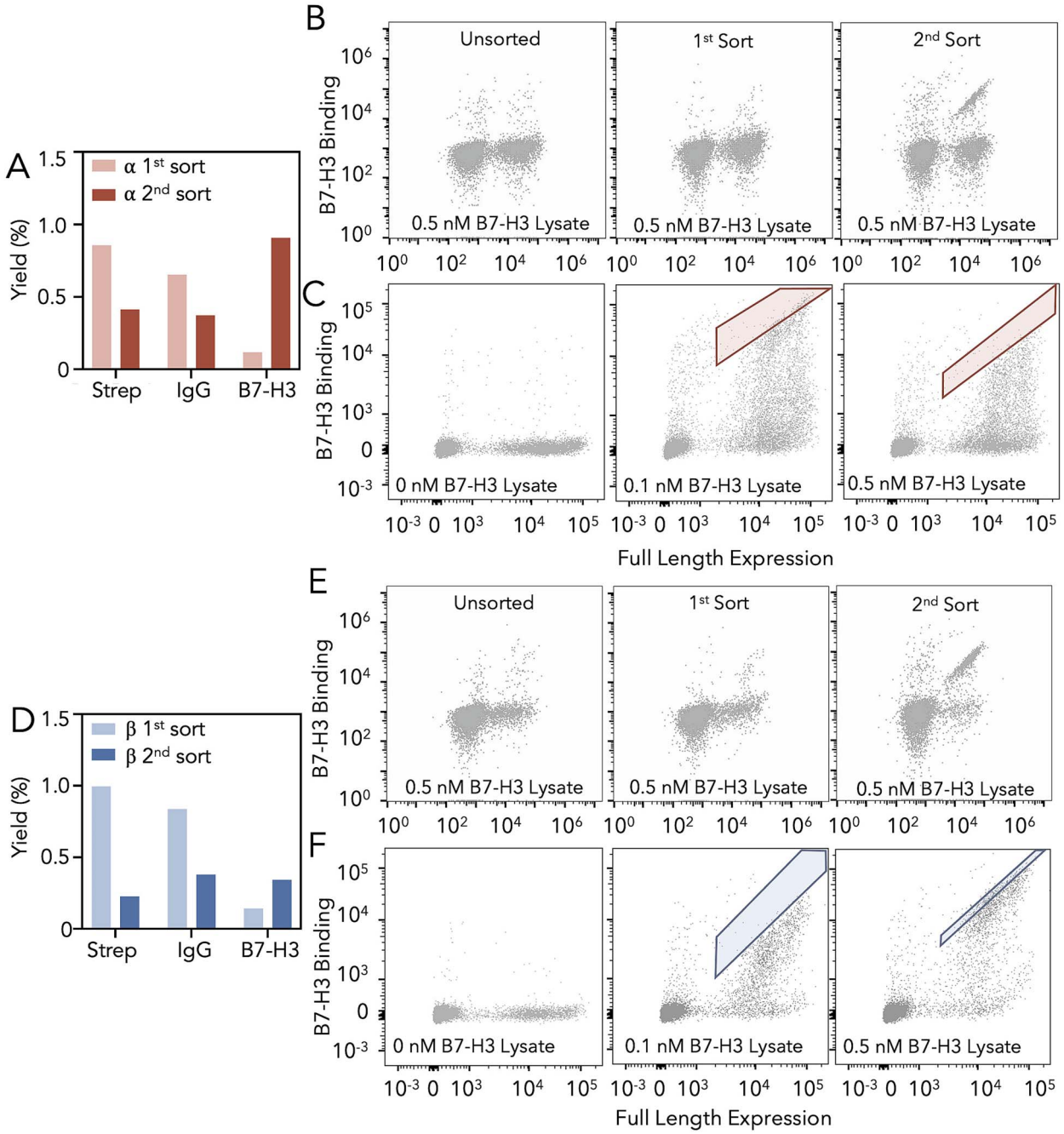
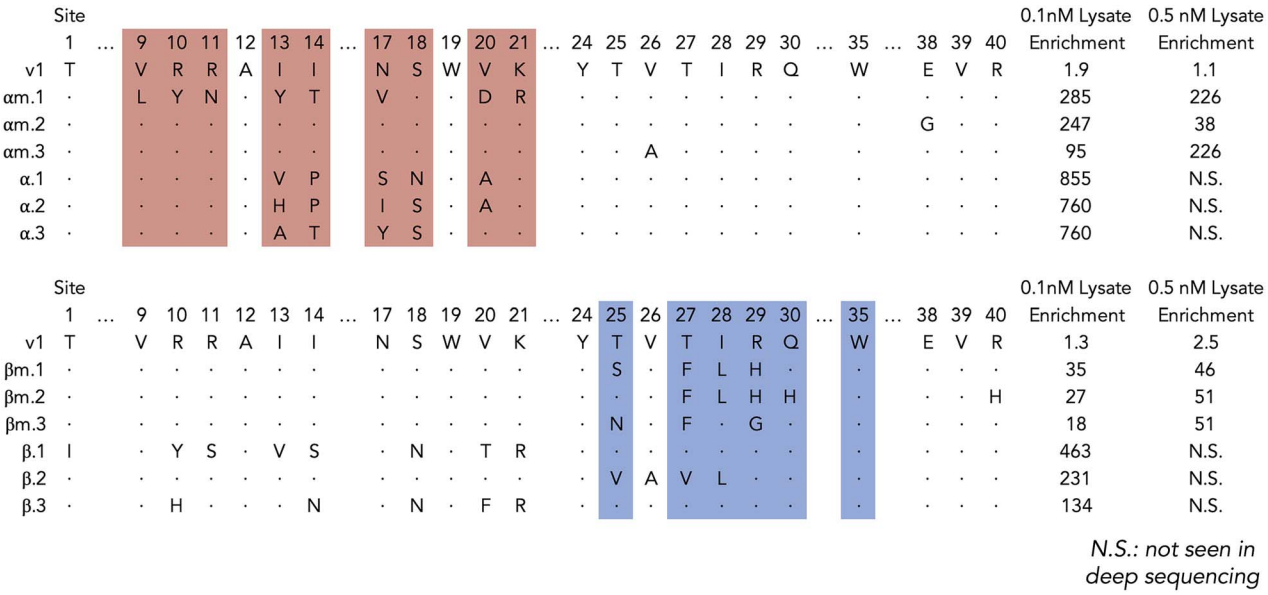


Figure 2 α and β library affinity maturation selections *via* yeast surface display. (A,D) yeast libraries displaying $\beta\alpha\beta\beta$ variants diversified at the α paratope (A) or β paratope (D) were depleted for streptavidin (strep) binders and immunoglobulin G (IgG) binders, followed by enrichment for B7-H3 lysate binding on magnetic beads. Yields from both magnetic bead sorts are plotted for the depletion and enrichment selections. (B, E) The unsorted, singly-sorted, and doubly-sorted populations were treated with 0.5 nM biotinylated B7-H3 lysate for the α library (B) or β library (E) followed with chicken anti-c-myc-fluorescein (FITC) and streptavidin-AlexaFluor647 (strep-A647) and analyzed by flow cytometry. (C,F) The resulting B7-H3 binders from the two magnetic bead sorts were then treated with 0.1 or 0.5 nM biotinylated B7-H3 lysate for the α library (C) or β library (F) followed with chicken anti-c-myc-FITC and strep-A647 for cell sorting *via* flow cytometry (middle and right panels respectively). Control samples, 0 nM B7-H3 lysate, shown in left panels. Gates selected for deep sequencing analysis highlighted in shaded boxes.

IgG depletion followed with enrichment for binding to 0.1 nM B7-H3 cell lysate, which resulted in preferential binding to B7-H3 over non-specific targets for both libraries (Fig. 2A and D). Flow cytometry analysis showed that yeast populations were enriched for strong binders to B7-H3 (Fig. 2B and E). At this stage, the populations were further enriched for B7-H3 binding *via* a set of parallel FACS with 0.1 nM and 0.5 nM B7-H3 lysate. Sorting populations at both B7-H3 lysate concentrations ensured strong binder discovery, *i.e.* if the 0.1 nM sort was too stringent or yielded a clonal population, the 0.5 nM sort would result in expanded lead sequences and additional site-wise amino acid information. Additionally, the 0.5 nM B7-H3 sort served as an intrinsic validation



Site	1	…	9	10	11	12	13	14	…	17	18	19	20	21	…	24	25	26	27	28	29	30	…	35	…	38	39	40	0.1nM Lysate Enrichment	0.5 nM Lysate Enrichment
v1	T		V	R	R	A	I	I		N	S	W	V	K		Y	T	V	T	I	R	Q		W		E	V	R	1.9	1.1
αm.1	·		L	Y	N	·	Y	T		V	·	·	D	R		·	·	·	·	·	·	·		·		·	·	·	285	226
αm.2	·		·	·	·	·	·	·		·	·	·	·	·		·	·	·	·	·	·	·		·		G	·	·	247	38
αm.3	·		·	·	·	·	·	·		·	·	·	·	·		·	·	A	·	·	·	·		·		·	·	·	95	226
α.1	·		·	·	·	·	V	P		S	N	·	A	·		·	·	·	·	·	·	·		·		·	·	·	855	N.S.
α.2	·		·	·	·	·	H	P		I	S	·	A	·		·	·	·	·	·	·	·		·		·	·	·	760	N.S.
α.3	·		·	·	·	·	A	T		Y	S	·	·	·		·	·	·	·	·	·	·		·		·	·	·	760	N.S.

Site	1	…	9	10	11	12	13	14	…	17	18	19	20	21	…	24	25	26	27	28	29	30	…	35	…	38	39	40	0.1nM Lysate Enrichment	0.5 nM Lysate Enrichment
v1	T		V	R	R	A	I	I		N	S	W	V	K		Y	T	V	T	I	R	Q		W		E	V	R	1.3	2.5
βm.1	·		·	·	·	·	·	·		·	·	·	·	·		·	S	·	F	L	H	·		·		·	·	·	35	46
βm.2	·		·	·	·	·	·	·		·	·	·	·	·		·	·	·	F	L	H	H		·		·	·	H	27	51
βm.3	·		·	·	·	·	·	·		·	·	·	·	·		·	N	·	F	·	G	·		·		·	·	·	18	51
β.1	I		·	Y	S	·	V	S		·	N	·	T	R		·	·	·	·	·	·	·		·		·	·	·	463	N.S.
β.2	·		·	·	·	·	·	·		·	·	·	·	·		·	V	A	V	L	·	·		·		·	·	·	231	N.S.
β.3	·		·	H	·	·	·	N		·	N	·	F	R		·	·	·	·	·	·	·		·		·	·	·	134	N.S.

N.S.: not seen in deep sequencing

Figure 3 Lead hit identification from deep sequencing analysis. Sequences of strongly enriched variants from each campaign are presented as alignments with parental v1.

of the lead candidates, as binders in the more stringent 0.1 nM sort should also be seen in the 0.5 nM populations. All sorts gave strong, specific B7-H3 binders relative to the 0 nM control (Fig. 2C and F). From the α 0.1 nM FACS the top 0.4% of B7-H3 binders were collected, while the top 0.8% were collected from the 0.5 nM FACS (Fig. 2C). For the β library the top 0.4% and 0.6% of B7-H3 binders were collected for the 0.1 nM and 0.5 nM FACS, respectively (Fig. 2F). All yeast collected in the gates shown in Fig. 2C and F were collected and DNA extracted for sequencing analysis.

Deep sequencing analysis and lead variant selection

Variant enrichments were calculated as the ratio of frequencies from the sorted *versus* unsorted populations *via* deep sequencing. Lead sequences were selected based on top enrichment scores from the 0.1 nM and 0.5 nM gates for each library. Not all sequences enriched in the 0.1 nM population were observed in the 0.5 nM populations for the α or β libraries. Thus, to maximize strong binding likelihood, we first selected variants with the top enrichment scores in 0.1 nM gate that were enriched $\geq 2\times$ in the 0.5 nM gate for either the α or β libraries, hereafter distinguished as αm or βm variants (Fig. 3). The top three variants, excluding sequences containing cysteine (to avoid unintentional disulfide formation) or single point mutations away from other top sequences, from the αm and βm populations were selected to be recombinantly expressed. Additionally, the top three enriched sequences seen in only the 0.1 nM gate for the α and β libraries were expressed recombinantly (Fig. 3) and are denoted as α or β variants. Notably, v1 was captured in the sequencing results for both concentrations of B7-H3 and for both libraries (Fig. 3), however with minimal enrichments as compared to the lead variants selected, thereby suggesting improved performance of new variants.

The most consistent mutations in this subset of variants are T27F and I28L. The T27F mutation was enriched in the β library binders at the most stringent 0.1 nM B7-H3 binding selection (Supplemental Fig. 4C) and was observed in all three of the variants that were most enriched in the 0.1 nM sorted population while also being enriched in the 0.5 nM population (*i.e.* the βm set; Fig. 3); conversely, parental I28 was generally conserved albeit not in the most enriched variants. These mutations are part of the ^{27}FLH^{29} motif within the two most enriched variants in the expanded β paratope. In addition, Q30 and W35 are consistently conserved from parental v1 in both lead variants (Fig. 3) and population-level analysis (Supplemental Fig. 4). Within the α paratope, there is a trend toward conservation of parental amino acids, both in the most enriched variants and the population-level analysis.

Lead variant characterization

Lead variants were cloned into *Escherichia coli* T7 Express, recombinantly produced, and purified from the soluble fraction. Five of 12 variants were obtained at 1–4 mg/L yield with 9 of 12 at $\geq$0.6 mg/L; αm.1, α.1 and α.2 exhibited poor yields and were excluded from further characterization (Supplemental Table 3). Variants were preliminarily evaluated for binding on MS1$^{B7\text{-}H3}$ cells. Three variants from the merged sort analysis, αm.2, βm.1 and βm.2, provided the strongest signals and were moved forward for full binding curve analysis (Supplemental Fig. 5). Subsequent titrations measured K_ds for these variants. βm.1 was the most potent binder, with a $K_d = 1.2$ nM [95% confidence interval: 1.0–1.4 nM; Fig. 4A]. The K_d values were 8.3 nM [5.4–13 nM] for αm.2 and 11 nM [3.1–27 nM] for βm.2 (Fig. 4A). As both βm.1 and αm.2 yielded K_d values within the desired single-digit nanomolar range, no further variants were characterized for K_d values. The parental v1 exhibited weaker affinity ($K_d > 100$ nM) for cell-intact B7-H3 relative to its 11 ± 5 nM for recombinant soluble extracellular domain (Blanchard *et al.* 2023). Thus, the 1.2 nM affinity for βm.1 corresponds to $>83\times$ improvement in potency over parental v1.

Specificity of lead variants to B7-H3 was evaluated by assessing binding of 100 nM ligand to two cell lines with low B7-H3 expression: the wild-type (WT) of our MS1 cell line (MS1^{WT}) and a

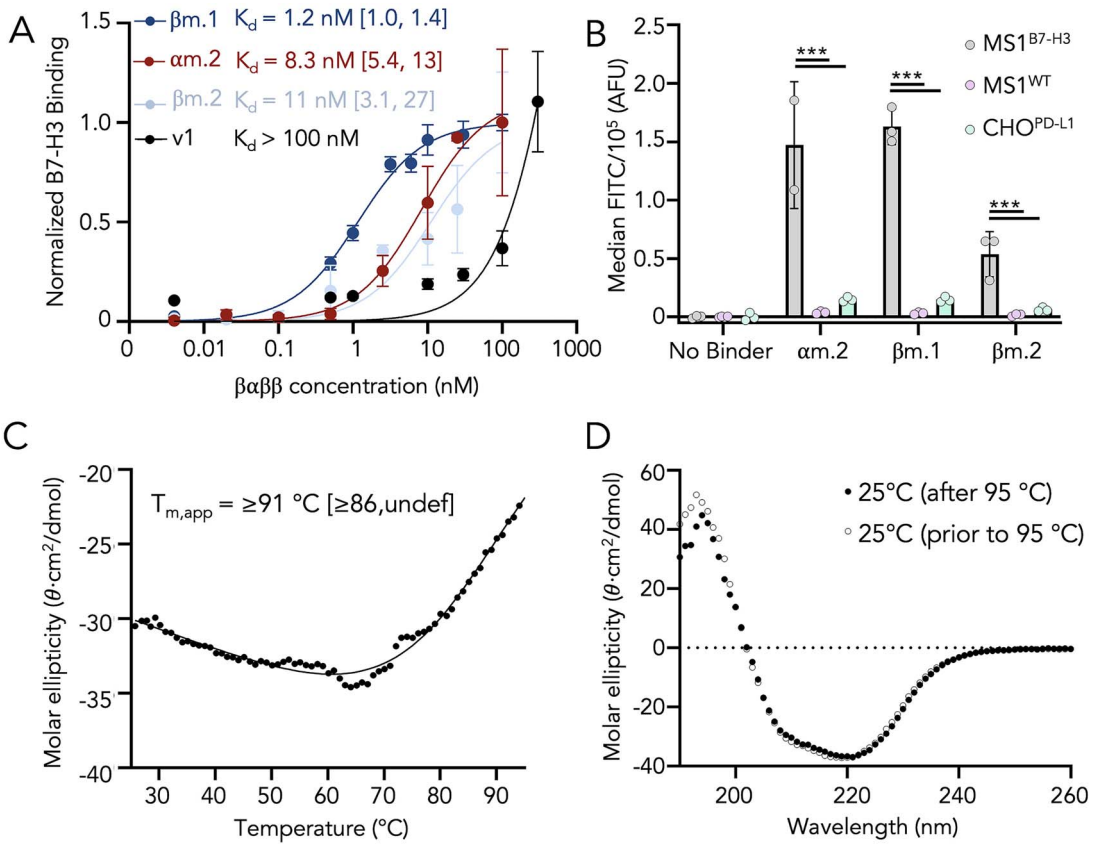


Figure 4 Characterization of lead variants. (A) Purified top variants, βm.1, αm.2, and βm.2, along with parental v1, were titrated onto MS1$^{B7\text{-}H3}$ cells, and relative binding was measured *via* rabbit anti-His$_6$-FITC labeling with flow cytometry. Data points are shown as mean ± standard deviation of at least three biological replicates. Modeled binding curves fit using a non-equilibrium single site binding model using GraphPad prism 9 are shown. (B) Specific binding was assessed by treating MS1$^{B7\text{-}H3}$, MS1^{WT}, and CHO$^{PD\text{-}L1}$ cells with 100 nM of lead $\beta\alpha\beta\beta$ variants. All data points were background subtracted. Statistical analysis between cell lines were completed with a two-way ANOVA with Tukey's correction, p-value *** <0.001. (C) The apparent midpoint of thermal denaturation ($T_{m,app}$) was determined by CD spectroscopy for βm.1 *via* measurement of molar ellipticity at 218 nm from 25–95°C. (D) Overlay of CD spectral scans, from 190–260 nm, of βm.1 at 25°C before and after 95°C.

CHO cell line overexpressing the cancer biomarker programmable death ligand 1 (PD-L1, CHO$^{PD\text{-}L1}$) (Supplemental Table 2) (Chatterjee *et al.* 2016). PD-L1, also known as B7-H1, is a member of the B7 family of proteins and therefore plays a role in altering T-cell activity.(Collins *et al.* 2005) While minimal, distinct binding above background was detected for the CHO$^{PD\text{-}L1}$ cell line for αm.2 and βm.1; future work will be needed to determine the molecular basis of this binding. However, at ~10× the affinity of αm.2 and βm.2, and 67× the affinity of βm.1, all molecules retain high specificity to cellular B7-H3 (Fig. 4B).

As βm.1 exhibited the single-digit nanomolar potency and the high specificity we desire in a lead molecule, we further characterized its stability. The apparent midpoint of thermal denaturation ($T_{m,app}$) was measured at ≥91°C [95% confidence interval: ≥86°C] (Fig. 4C) which is an increase relative to v1, with a reported $T_{m,app}$ of ≥88°C (Blanchard *et al.* 2023). Due to the limitations in reaching temperatures ≥100°C when measuring the thermal denaturation *via* CD, a clear plateau for the fully denatured form for proteins with elevated $T_{m,app}$ is not observed. We therefore report the lowest possible $T_{m,app}$ based on data collected, but also report that the $T_{m,app}$ may be greater, as it cannot be measured precisely. After thermal treatment, βm.1 refolds to its native structure (Fig. 4D). Additionally, this $T_{m,app}$ is greater than the thermal requirements for typical radioligand conjugation reactions (Huclier-Markai *et al.* 2014), thus securing it as a strong candidate.

Structural modeling analysis

We utilized AF3 to predict where βm.1 would engage B7-H3. An overlay between v1 and βm.1 with B7-H3 suggests engagement with B7-H3 at the same epitope with the same relative orientation, albeit with moderate confidence for the v1 interface (iPTM = 0.53) relative to the βm.1 interface (iPTM = 0.78), thereby acknowledging the resultant structures as hypothetical possibilities (Fig. 5A). T27F is a non-homologous mutation in the heart of the predicted $\beta\alpha\beta\beta$ / B7-H3 interface (Fig. 5B). The T72 and Q74 side chains from B7-H3 lie in a plane nearly perpendicular to the F27 phenyl ring and 2.8 Å from its edge (Fig. 5C), thereby creating substantially different engagement than the parental T27. The T27F mutation was enriched in the β 0.1 nM population (Supplemental Fig. 4C). A second aromatic, W35, maintained its side chain from parental v1. The side chain likely engages the $\beta\alpha\beta\beta$ hydrophobic core and extends to engage sites 66 (I) and 123 (F) on B7-H3. The other site that was diversified in the β library yet appeared conserved within βm.1 was Q30, which seemingly retained its engagement with

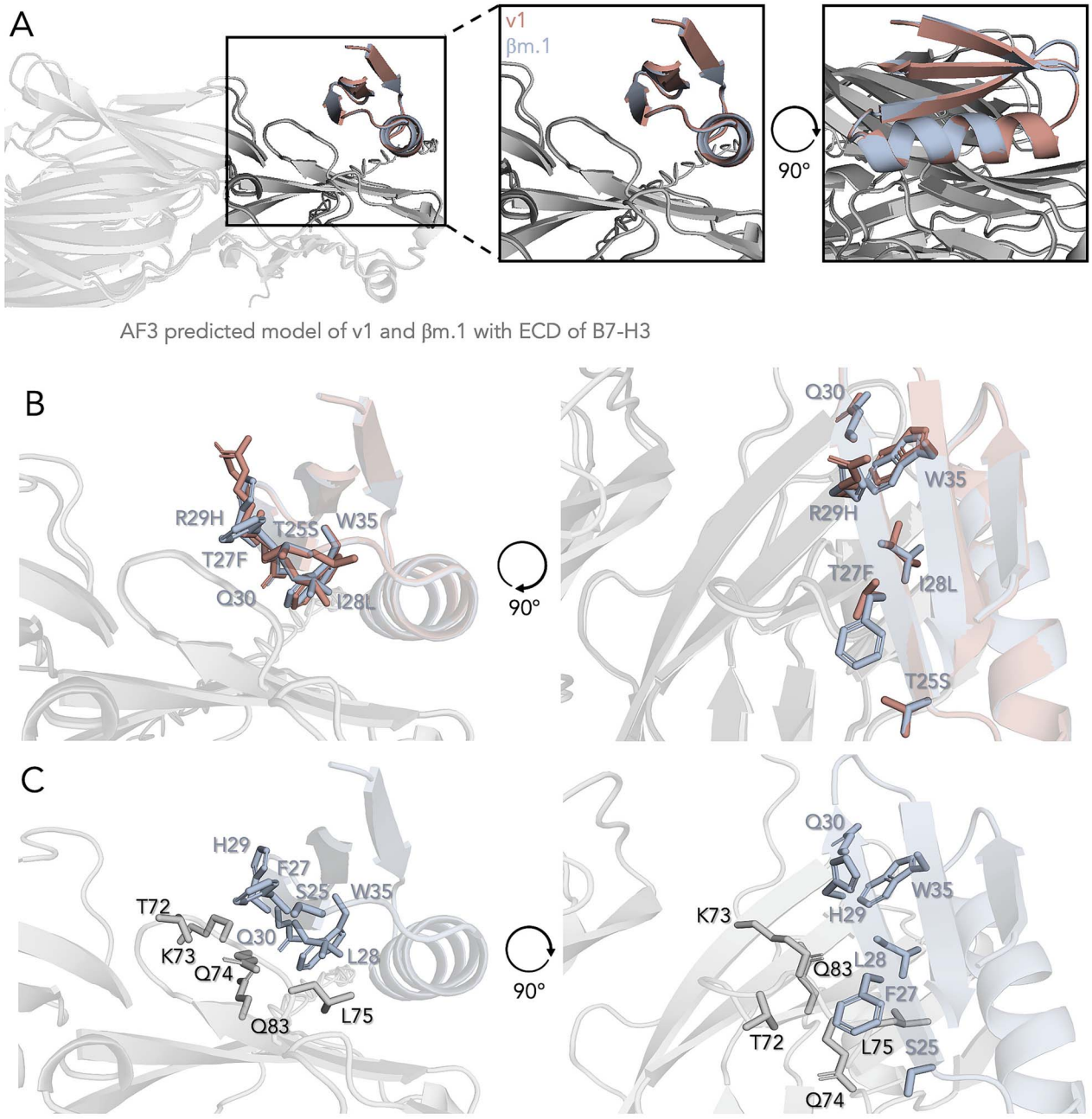


Figure 5 Structural analysis of βm.1. (A) AlphaFold3 (AF3) predicted structure of βm.1 (light blue) and B7-H3 extracellular domain (1–456, light grey) binding overlaid with v1 (light red) binding to B7-H3 ECD (dark grey). pTM = 0.47 and 0.41; ipTM = 0.78 and 0.53 for βm.1 and v1 respectively. (B) Mutations for βm.1 from parental v1 shown in light red, βm.1 shown in light blue and B7-H3 shown in light grey. (C) Side chains of βm.1 (light blue) shown with side chains of B7-H3 ECD (light grey) residues within 4 Å.

F129 on B7-H3. These conservations align well with the site-wise amino acid enrichments for Q30 and W35 as they are enriched at these sites in the β library in both sorts (Supplemental Fig. 4C and D). The three other mutations were relatively homologous with potential impacts on target interface, core packing, and solvent engagement. T25S is a homologous mutation that prunes the methyl group in the threonine side chain, which is reasonable in light of the side chain's potential interaction with solvent (81% relative SASA of the T25 side chain). I28L is a homologous mutation at a buried site (31% SASA in unbound state) that could modify core packing. R29H is a moderately homologous mutation. The resultant side chain seemingly engages the alkyl component of K73 on B7-H3.

Since βm.1 and v1 show similar positioning on B7-H3 in the proposed structures, and our design included the β library to engage the β-sheet with B7-H3, we again used AF3 to predict engagement for additional enriched variants. AF3 predicted, with limited confidence, that β library variants bind in a manner akin to v1 and βm.1 (Supplemental Fig. 6). However, the enriched α library variants are predicted, with limited confidence, to bind to varied regions of B7-H3 (Supplemental Fig. 7). Additionally, the expected conformation of B7-H3 is altered throughout the various

binding modes of the α library variants where the β library variants all exhibit the same B7-H3 predicted conformer.

Discussion

Radioligand therapy is a powerful cancer treatment but requires additional ligands to extend the breadth and depth of cancer patient populations able to be treated. To directly address this, as well as to engineer an advanced B7-H3 ligand for other molecular targeting applications, we engineered hyperstable $\beta\alpha\beta\beta$ miniproteins targeting B7-H3, a well-validated and important cancer biomarker (Collins *et al.* 2005; Zhou and Jin, 2021; Zafar *et al.* 2025). We improved affinity to 1.2 nM and thermal stability to $T_{m,app} \geq 91°C$, including reversible unfolding. Affinity maturation was empowered by structure-guided evolution. While diversification of the originally engineered α-helix paratope yielded a variant with improved 8.5 nM affinity, greater improvement was achieved in recognizing that portions of the β-sheet putatively engaged with B7-H3 in the parental $\beta\alpha\beta\beta$ miniprotein (Fig. 1B). Inclusion of these residues proved capable of driving affinity, as our most performant molecule, βm.1, stemmed from the β library with four mutations within the β-sheet. Broad diversification at several β-sheet sites was key as a highly non-homologous mutation, T27F, appears in the top variant. Moreover, structural analysis indicates key engagement of T27F with B7-H3. Additionally, even without the presence of a stability selection, our lead variant advanced the high stability ($T_{m,app} \geq 91°C$) seen in parental v1 and characteristic of synthetic $\beta\alpha\beta\beta$ miniproteins (Rocklin *et al.* 2017). Parallel sorting at two sub-nanomolar concentrations of B7-H3 lysate aided identification of top performing variants as these αm or βm variants exhibited the strongest binding in clonal characterization. The only exception was αm.1, which was not readily produced in the soluble fraction (although no troubleshooting was pursued because of the wealth of other variants). Intriguingly, in both the bound complex between αm.1 and B7-H3 and in isolation, AF3 does not predict αm.1 into the canonical $\beta\alpha\beta\beta$ fold, but rather two pairs of β-sheets linked together *via* flexible loops (Supplemental Fig. 8A and B). Poor folding of αm.1 could result in minimal to no soluble expression coinciding with our inability to produce this variant.

While the original evolutionary plan considered the potential to merge beneficial mutations in both the α-helix and β-sheet, the reduced improvement in the α-helix, as well as the predicted modification of binding orientation, dampen enthusiasm for the strategy in this case. Additional future libraries may focus on expanding the breadth of residues allowed on the β-sheet, thus furthering the putative engagement this addition yielded. Even greater breadth, in both sites and amino acid options, could be achieved with random mutagenesis (*e.g. via* error-prone PCR); yet such an expanded search results in necessary undersampling of the immense sequence space. Improved variants could be also obtained through alternating stability selections rather than exclusively affinity maturation. Overall, the affinity campaign yielded relatively few hits and thus expansion in library design may be relevant to pursue picomolar level binders. Nevertheless, the performance goals set out within this campaign were met – with 1.2 nM affinity, specificity, and $\geq 91°C$ thermal stability – within β-sheet engineering. The results suggest the potential for a new $\beta\alpha\beta\beta$ library design for *de novo* discovery in which sites on both the α-helix and β-sheet are diversified simultaneously. In our previous work (Blanchard *et al.* 2023), we have shown that diversification of either paratope *separately* can yield strong, selective binders with hyperstability. A hybrid α/β paratope would be a compelling addition to a library of libraries strategy. Expanding the diversified paratope in a 40-residue miniprotein runs the risk of destabilization, even from a hyperstable starting point. Thus, sitewise constraints on diversification may be valuable (Woldring *et al.* 2015, 2017; Kruziki *et al.* 2018). Deep sequencing of performant mutant populations, such as performed here, will provide valuable data for such constraint.

Previous work related to receptor-targeting applications suggest that low single-digit nanomolar affinities are beneficial relative to weaker affinities and often sufficient for successful therapies (Adams *et al.* 2001; Thurber and Wittrup, 2008; Schmidt and Wittrup, 2009; Zahnd *et al.* 2010; Okarvi and Jammaz, 2012; Orcutt *et al.* 2012; Tolmachev *et al.* 2012). Therefore, achieving with 1.2 nM affinity and specificity for B7-H3 alongside $\geq 91°C$ thermal stability successfully places βm.1 as a lead candidate for radioligand therapy. Future studies will focus on site-specific conjugation of βm.1 with a peptide linker followed by ^{177}Lu radiolabeling (*via* DOTA). Radiolabeled βm.1 can then be studied for tumor reduction, survival, and specificity to B7-H3 in a murine model.

Materials and methods

Additional materials and methods describing general DNA methods, cell culturing and variant production can be found in the supplemental information.

Library assembly and yeast electroporation

Saccharomyces cerevisiae EBY100 yeast were transformed *via* electroporation as done previously (Chen *et al.* 2013b). In brief, *S. cerevisiae* EBY100 were grown until an optical density at 600 nm (OD_{600}) of ~1.3–1.5, washed with cold sterile deionized water twice, followed by a wash of cold buffer E (1.0 M sorbitol, 1 mM calcium chloride). Cells were then resuspended in lithium acetate solution (0.1 M lithium acetate, 10 mM tris(hydroxymethyl)aminomethane, 1 mM ethylenediaminetetraacetic acid, 10 mM dithiothreitol, pH 7.5) for 30 min at 30°C, 250 RPM. Cells were washed with cold buffer E and then resuspended in buffer E along with purified gene insert (200 pmol) and linear pCT vector (6 μg). Cells were then electroporated at 1.2 kV and 25 μF and grown in YPD for 1 hr prior to SD-CAA selection for 16 hr at 30°C, 250 RPM. Library diversities were calculated based on the OD_{600} after 16 hrs of growth (30°C, 250 RPM) in SD-CAA media and confirmed *via* colony-forming units (CFU) on SD-CAA plates. 20× the calculated diversity of each library were induced with SG media.

Monovalent MACS selections and mammalian cell lysate preparation

For the first round of MACS selection, 20× the library diversity of the induced yeast display library was resuspended in 2 mL phosphate-buffered saline (PBS) supplemented with 1 g/L bovine serum albumin (PBSA). Two depletions of non-specific binders were performed, first with 10 μL of Dynabeads Biotin Binder

magnetic beads (Thermo Scientific), followed by magnetic beads coated with biotinylated goat IgG (Rockland 005–0602). Depletions were performed for 2 hrs, rotating at 4°C, and bound yeast were removed and quantified *via* CFU on YPD plates. B7-H3 receptors were quantified on $MS1^{B7\text{-}H3}$ cells with Quantum Simply Cellular anti-mouse IgG beads (Bangs Laboratories 815A) with mouse anti-CD276(B7-H3)-PE (Biolegend, 331 605). $MS1^{B7\text{-}H3}$ cells were labeled with 0.05 g/L of Sulfo-NHS-LC-biotin (Thermo Scientific, cat. no. 21335) in 750 μL PBS for 30 min, rotating at room temperature. Biotinylation was quenched with two washes of PBSA (1 mL). Cell count and average receptor count of 3.06x10^5 receptors/cell were used to estimate the nanomolar concentration of B7-H3 daily for each experiment. Cells were resuspended in 750 μL of lysis buffer (PBS with 1% v/v Triton X-100, 2 mM EDTA and 1× protease inhibitor tablet, pH 7.4) and incubated for 25 min, rotating at 4°C. Soluble lysate was obtained by centrifugation (20 000 *g*, 4°C, 20 min) and diluted with PBSA for a final concentration of 0.5 nM biotinylated B7-H3 (final v/v lysis buffer/PBSA $\leq$2%). Unbound yeast from the IgG depletion were resuspend in biotinylated B7-H3 lysate and incubated for 2 hr, rotating, 4°C. Cells were centrifuged (8000 *g*, 1 min), washed with PBSA (1 mL), and captured with 10 μL of Dynabeads Biotin Binder magnetic beads. Bound yeast were removed, resuspended in SD-CAA, and grown for 12–16 hr, quantified *via* OD_{600} and confirmed with CFU on YPD plates. For the second round of MACS, 10× the theoretical diversity of the singly-sorted libraries were depleted against biotin beads, followed by IgG beads and then enriched for B7-H3 binders with 0.1 nM biotinylated B7-H3 lysate.

FACS selections

For the FACS affinity selection, yeast were incubated with either 0.1 or 0.5 nM biotinylated B7-H3 lysate and chicken anti-c-myc-FITC (ICL Labs, CMYC-45F-Z), followed by streptavidin-AF647 (Invitrogen S32357). Yeast exhibiting the strongest binding:display ratio were collected (Fig. 2C and F). All FACS selections were performed using a FACS Aria II at the University of Minnesota Flow Cytometry Core facility. Collected yeast were resuspended in SD-CAA media and grown until 20× the theoretical diversity was reached.

Deep sequencing preparation and analysis

Yeast collected from each gate during FACS underwent plasmid extraction as follows: 1x10^8 cells in mid-log phase were resuspended in Zymolyase solution 1 (50 mM phosphate buffer, 1 M sorbitol, 10 mM β-mercaptoethanol, 0.24 U/μL Zymolyase (Zymo Reasearch), pH 7.5) at 37°C, shaking for 30 min. Followed by a GenCatch plasmid extraction according to the manufacturers protocol. Plasmid DNA from each population was amplified by standard PCR with Q5 Master Mix (New England Biolabs) to incorporate barcoded DNA regions for AVITI sequencing. PCR products were confirmed *via* gel electrophoresis and purified *via* extraction (Zymoclean Gel DNA Recovery Kit) and sequenced by the University of Minnesota Genomics Center. AVITI sequencing resulted in general read lengths of 151 bp with 9x10^4 and 6×10^5 reads of the unsorted α and β libraries and 8×10^4–2×10^6 (average: 7×10^5) reads for the sorted populations. Raw reads were merged, filtered, and translated, and unique sequences were combined using USEARCH (Edgar, 2010). Enrichment was computed as the ratio of frequencies between the sorted and unsorted populations. As the large sizes of the unsorted populations resulted in incomplete coverage, the initial frequency was approximated as the inverse of the theoretical diversity.

Affinity titrations

0.5-2 $\times 10^5$ $MS1^{B7\text{-}H3}$ cells were labeled with varying concentrations of purified $\beta\alpha\beta\beta$ at 4°C with agitation. Cells were washed with cold PBSA and labeled with rabbit anti-His_6-FITC (Abcam ab1206) for 30 minutes at 4°C, rotating. Cells were washed, and the median fluorescence was measured *via* flow cytometry. The background signal from a sample without $\beta\alpha\beta\beta$ was subtracted. The k_{off} of each $\beta\alpha\beta\beta$ was determined under non-equilibrium conditions by minimizing the sum of squared error in a non-equilibrium binding model in GraphPad Prism 9 based on the incubation time using a k_{on} approximation of 2.5×10^5 M^{-1} sec^{-1} (Wojcik *et al.* 2010). All samples were normalized to their same-day maximum fluorescence.

Apparent midpoint of thermal denaturation

The apparent midpoint of thermal denaturation ($T_{m,app}$) was determined by circular dichroism (CD). Purified protein in 10 mM phosphate buffer (0.341 g/L sodium dihydrogen phosphate, 1.015 g/L sodium phosphate dibasic, pH 7.4) was diluted to ~0.1 g/L in phosphate buffer, and the thermal stability and secondary structure were measured *via* CD using a JASCO J-815 CD spectropolarimeter (Biophysical Technology Center, University of Minnesota). Thermal stability was measured by monitoring ellipticity at 218 nm as temperature increased from 25 to 95°C with a 3°C/min ramp. Melting temperatures were determined using two-state unfolding equation and minimizing the sum of squared errors between predicted and empirical data (Hackel *et al.* 2008). Spectra were obtained by scanning from 260 to 190 nM at 25°C before thermal treatment.

AlphaFold structural analysis, additional figure generation and statistical testing

AF3 structures were generated using the AlphaFold server with default settings (Abramson *et al.* 2024). B7-H3 sequence was truncated to only include the extracellular domains (UniProt: Q5ZPR3, residues 1–456). Flow cytometric overlay plots were generated using FlowJo 10. All bar plots were generated with GraphPad Prism 9, and statistical analysis was completed in GraphPad Prism 9.

Acknowledgements

We would like to thank the University Flow Cytometry Resource at the University of Minnesota, the University of Minnesota Genomics Center, the University of Minnesota Biophysical Technology Center, and the Minnesota Supercomputing Institute for their expertise and access to their resources.

Author contributions

Hannah Windsor (Conceptualization [equal], Data curation [lead], Formal analysis [lead], Investigation [lead], Methodology [equal],

Writing - original draft [lead], Writing - review & editing [equal]), Nicholas C Ulen (Formal analysis [supporting], Investigation [supporting], Writing - review & editing [supporting]), Claudia Beaudry (Formal analysis [supporting], Investigation [supporting], Writing - review & editing [supporting]), Benjamin J Hackel (Conceptualization [equal], Formal analysis [supporting], Funding acquisition [lead], Methodology [equal], Project administration [lead], Writing - original draft [supporting], Writing - review & editing [equal]).

Conflict of interest

HW and BJH are inventors on a patent application related to the proteins in this study.

Funding

We appreciate support from the Randy Shaver Cancer and Community Fund and NIH R01 (GM146372).

Data availability

The data underlying this article are available in the article and in its online supplementary material. Any additional details will be readily provided upon request to the corresponding author.

References

Abramson J, Adler J, Dunger J *et al.* Accurate structure prediction of biomolecular interactions with AlphaFold 3. *Nature* 2024;630:493–500. https://doi.org/10.1038/s41586-024-07487-w.

Adams GP, Schier R, McCall AM *et al.* High affinity restricts the localization and tumor penetration of single-chain fv antibody molecules. *Cancer Res* 2001;61:4750–5.

Arigami T, Narita N, Mizuno R *et al.* B7–H3 ligand expression by primary breast cancer and associated with regional nodal metastasis. *Ann Surg* 2010;252:1044–51. https://doi.org/10.1097/SLA.0b013e3181f1939d.

Baker EG, Bartlett GJ, Porter Goff KL *et al.* Miniprotein design: Past, present, and prospects. *Acc Chem Res* 2017;50:2085–92. https://doi.org/10.1021/acs.accounts.7b00186.

Blanchard PL, Knick BJ, Whelan SA *et al.* Hyperstable synthetic mini-proteins as effective ligand scaffolds. *ACS Synth Biol* 2023;12:3608–22. https://doi.org/10.1021/acssynbio.3c00409.

Ceeraz S, Nowak E, Noelle R. B7 family checkpoint regulators in immune regulation and disease. *Trends Immunol* 2013;34:556–63. https://doi.org/10.1016/j.it.2013.07.003.

Chatterjee S, Lesniak WG, Gabrielson M *et al.* A humanized antibody for imaging immune checkpoint ligand PD-L1 expression in tumors. *Oncotarget* 2016;7:10215–27. https://doi.org/10.18632/oncotarget.7143.

Chen J, Sawyer N, Regan L. Protein–protein interactions: General trends in the relationship between binding affinity and interfacial buried surface area. *Protein Sci* 2013a;22:510–5. https://doi.org/10.1002/pro.2230.

Chen TF, de Picciotto S, Hackel BJ *et al.* In: Keating AE (ed.), *Methods in Enzymology*: Academic Press, San Diego, 2013b, pp. 303–26.

Cherf GM, Cochran JR. Applications of yeast surface display for protein engineering. *Methods Mol Biol Clifton NJ* 2015;1319:155–75. https://doi.org/10.1007/978-1-4939-2748-7_8.

Chow HY, Zhang Y, Matheson E *et al.* Ligation Technologies for the Synthesis of cyclic peptides. *Chem Rev* 2019;119:9971–10001. https://doi.org/10.1021/acs.chemrev.8b00657.

Collins M, Ling V, Carreno BM. The B7 family of immune-regulatory ligands. *Genome Biol* 2005;6:223. https://doi.org/10.1186/gb-2005-6-6-223.

Condado-Morales I, Dingfelder F, Waibel I *et al.* A comparative study of the developability of full-length antibodies, fragments, and bispecific formats reveals higher stability risks for engineered constructs. *mAbs* 2024;16:2403156. https://doi.org/10.1080/19420862.2024.2403156.

Dudgeon K, Rouet R, Kokmeijer I *et al.* General strategy for the generation of human antibody variable domains with increased aggregation resistance. *Proc Natl Acad Sci* 2012;109:10879–84. https://doi.org/10.1073/pnas.1202866109.

Edgar RC. Search and clustering orders of magnitude faster than BLAST. *Bioinformatics* 2010;26:2460–1. https://doi.org/10.1093/bioinformatics/btq461.

Fraczkiewicz R, Braun W. Exact and efficient analytical calculation of the accessible surface areas and their gradients for macromolecules. *J Comput Chem* 1998;19:319–33. https://doi.org/10.1002/(SICI)1096-987X(199802)19:3<319::AID-JCC6>3.0.CO;2-W.

Frejd FY, Kim KT. Affibody molecules as engineered protein drugs. *Exp Mol Med* 2017;49:e306. https://doi.org/10.1038/emm.2017.35.

Gai SA, Wittrup KD. Yeast surface display for protein engineering and characterization. *Curr Opin Struct Biol* 2007;17:467–73. https://doi.org/10.1016/j.sbi.2007.08.012.

Gerton JL, Ohgi S, Olsen M *et al.* Effects of mutations in residues near the active site of human immunodeficiency virus type 1 integrase on specific enzyme-substrate interactions. *J Virol* 1998;72:5046–55. https://doi.org/10.1128/JVI.72.6.5046-5055.1998.

Gurevich EV, Gurevich VV. Therapeutic potential of small molecules and engineered proteins. *Handb Exp Pharmacol* 2014;219:1–12. https://doi.org/10.1007/978-3-642-41199-1_1.

Hackel BJ, Kapila A, Wittrup KD. Picomolar affinity fibronectin domains engineered utilizing loop length diversity, recursive mutagenesis, and loop shuffling. *J Mol Biol* 2008;381:1238–52. https://doi.org/10.1016/j.jmb.2008.06.051.

Harding FA, Stickler MM, Razo J *et al.* The immunogenicity of humanized and fully human antibodies. *mAbs* 2010;2:256–65. https://doi.org/10.4161/mabs.2.3.11641.

He M, Taussig MJ. Rapid discovery of protein interactions by cell-free protein technologies. *Biochem Soc Trans* 2007;35:962–5. https://doi.org/10.1042/BST0350962.

Höppner J, Noda H, Anitha AK *et al.* Prolonging parathyroid hormone analog action in vitro and in vivo through peptide lipidation. *Nat Commun* 2025;16:4487. https://doi.org/10.1038/s41467-025-59665-7.

Huclier-Markai S, Kerdjoudj R, Alliot C *et al.* Optimization of reaction conditions for the radiolabeling of DOTA and DOTA-peptide with 44m/44Sc and experimental evidence of the feasibility of an in vivo PET generator. *Nucl Med Biol* 2014;41:e36–43. https://doi.org/10.1016/j.nucmedbio.2013.11.004.

Jaroszewicz W, Morcinek-Orłowska J, Pierzynowska K *et al.* Phage display and other peptide display technologies. *FEMS Microbiol Rev* 2022;46:fuab 052. https://doi.org/10.1093/femsre/fuab052.

Kintzing JR, Filsinger Interrante MV, Cochran JR. Emerging strategies for developing next-generation protein therapeutics for cancer treatment. *Trends Pharmacol Sci* 2016;37:993–1008. https://doi.org/10.1016/j.tips.2016.10.005.

Kruziki MA, Bhatnagar S, Woldring DR *et al.* A 45-amino-acid scaffold mined from the PDB for high-affinity ligand engineering. *Chem Biol* 2015;22:946–56. https://doi.org/10.1016/j.chembiol.2015.06.012.

Kruziki MA, Sarma V, Hackel BJ. Constrained combinatorial libraries of Gp2 proteins enhance discovery of PD-L1 binders. *ACS Comb Sci* 2018;20:423–35. https://doi.org/10.1021/acscombsci.8b00010.

Liu J, Pandya P, Afshar S. Therapeutic advances in oncology. *Int J Mol Sci* 2021;22:2008. https://doi.org/10.3390/ijms22042008.

Lowe D, Dudgeon K, Rouet R *et al. Aggregation, Stability, and Formulation of Human Antibody Therapeutics Academic*. Elsevier, Oxford, UK, 2011.

Lucana MC, Arruga Y, Petrachi E *et al.* Protease-resistant peptides for targeting and intracellular delivery of therapeutics. *Pharmaceutics* 2021;13:2065. https://doi.org/10.3390/pharmaceutics13122065.

Lutz AM, Bachawal SV, Drescher CW *et al.* Ultrasound molecular imaging in a human CD276 expression–modulated murine ovarian cancer model. *Clin Cancer Res* 2014;20:1313–22. https://doi.org/10.1158/1078-0432.CCR-13-1642.

McConnell A, Batten SL, Hackel BJ. Determinants of developability and evolvability of synthetic miniproteins as ligand scaffolds. *J Mol Biol* 2023;435:168339. https://doi.org/10.1016/j.jmb.2023.168339.

McGregor DP. Discovering and improving novel peptide therapeutics. *Anti-Infect Technol* 2008;8:616–9.

Miller CD, Lozada JR, Zorko NA *et al.* Pan-cancer interrogation of B7-H3 (CD276) as an actionable therapeutic target across human malignancies. *Cancer Res Commun* 2024;4:1369–79. https://doi.org/10.1158/2767-9764.CRC-23-0546.

Minati R, Perreault C, Thibault P. A roadmap toward the definition of actionable tumor-specific antigens. *Front Immunol* 2020;11:583287. https://doi.org/10.3389/fimmu.2020.583287.

Ninatti G, Lee ST, Scott AM. Radioligand therapy in cancer management: A global perspective. *Cancers* 2025;17:3412. https://doi.org/10.3390/cancers17213412.

Okarvi SM, Jammaz IA. Preparation and evaluation of bombesin peptide derivatives as potential tumor imaging agents: Effects of structure and composition of amino acid sequence on in vitro and in vivo characteristics. *Nucl Med Biol* 2012;39:795–804. https://doi.org/10.1016/j.nucmedbio.2012.01.002.

Orcutt KD, Rhoden JJ, Ruiz-Yi B *et al.* Effect of small-molecule–binding affinity on tumor uptake in vivo: A systematic study using a Pretargeted bispecific antibody. *Mol Cancer Ther* 2012;11:1365–72. https://doi.org/10.1158/1535-7163.MCT-11-0764.

Osuna S. The challenge of predicting distal active site mutations in computational enzyme design. *WIREs Comput Mol Sci* 2021;11:e1502. https://doi.org/10.1002/wcms.1502.

Ożga K, Berlicki Ł. Design and engineering of Miniproteins. *ACS Bio Med Chem Au* 2022;2:316–27. https://doi.org/10.1021/acsbiomedchemau.2c00008.

Passaro A, Al Bakir M, Hamilton EG *et al.* Cancer biomarkers: Emerging trends and clinical implications for personalized treatment. *Cell* 2024;187:1617–35. https://doi.org/10.1016/j.cell.2024.02.041.

Reinwarth M, Nasu D, Kolmar H *et al.* Chemical synthesis, backbone cyclization and oxidative folding of cystine-knot peptides — Promising scaffolds for applications in drug design. *Mol* 2012;17:12533–52.

Ribeiro R, Moreira JN, Goncalves J. Development of a new affinity maturation protocol for the construction of an internalizing anti-nucleolin antibody library. *Sci Rep* 2024;14:10608. https://doi.org/10.1038/s41598-024-61230-z.

Rocklin GJ, Chidyausiku TM, Goreshnik I *et al.* Global analysis of protein folding using massively parallel design, synthesis, and testing. *Science* 2017;357:168–75. https://doi.org/10.1126/science.aan0693.

Sartor O, De Bono J, Chi KN *et al.* Lutetium-177–PSMA-617 for metastatic castration-resistant prostate cancer. *N Engl J Med* 2021;385:1091–103. https://doi.org/10.1056/NEJMoa2107322.

Schmidt MM, Wittrup KD. A modeling analysis of the effects of molecular size and binding affinity on tumor targeting. *Mol Cancer Ther* 2009;8:2861–71. https://doi.org/10.1158/1535-7163.MCT-09-0195.

Senior M. Fresh from the biotech pipeline: Fewer approvals, but biologics gain share. *Nat Biotechnol* 2023;41:174–82. https://doi.org/10.1038/s41587-022-01630-6.

Sgouros G, Bodei L, McDevitt MR *et al.* Radiopharmaceutical therapy in cancer: Clinical advances and challenges. *Nat Rev Drug Discov* 2020;19:589–608. https://doi.org/10.1038/s41573-020-0073-9.

Shi X, Day A, Bergom HE *et al.* Integrative molecular analyses define correlates of high B7-H3 expression in metastatic castrate-resistant prostate cancer. *NPJ Precis Oncol* 2022;6:80. https://doi.org/10.1038/s41698-022-00323-2.

Smith GP, Petrenko VA. Phage display. *Chem Rev* 1997;97:391–410. https://doi.org/10.1021/cr960065d.

Stern LA, Lown PS, Kobe AC *et al.* Cellular-based selections aid yeast-display discovery of genuine cell-binding ligands: Targeting oncology vascular biomarker CD276. *ACS Comb Sci* 2019;21:207–22. https://doi.org/10.1021/acscombsci.8b00156.

Stern LA, Schrack IA, Johnson SM *et al.* Geometry and expression enhance enrichment of functional yeast-displayed ligands via cell panning. *Biotechnol Bioeng* 2016;113:2328–41. https://doi.org/10.1002/bit.26001.

Strosberg J, El-Haddad G, Wolin E *et al.* Phase 3 trial of177Lu-Dotatate for Midgut neuroendocrine Tumors. *N Engl J Med* 2017;376:125–35. https://doi.org/10.1056/NEJMoa1607427.

Thurber GM, Wittrup KD. A mechanistic compartmental model for total antibody uptake in tumors. *J Theor Biol* 2012;314:57–68. https://doi.org/10.1016/j.jtbi.2012.08.034.

Thurber GM, Wittrup KD. Quantitative spatiotemporal analysis of antibody fragment diffusion and endocytic consumption in tumor spheroids. *Cancer Res* 2008;68:3334–41. https://doi.org/10.1158/0008-5472.CAN-07-3018.

To J, Magid R, Cleland J *et al.* The landscape for radioligand therapies in oncology. *Nat Rev Drug Discov* 2025;24:584–5. https://doi.org/10.1038/d41573-025-00096-w.

Tolmachev V, Tran TA, Rosik D *et al.* Tumor targeting using affibody molecules: Interplay of affinity, target expression level, and

binding site composition. *J Nucl Med Off Publ Soc Nucl Med* 2012;53:953–60.

Ucisik MN, Hammes-Schiffer S. Effects of active site mutations on specificity of nucleobase binding in human DNA polymerase η. *J Phys Chem B* 2017;121:3667–75. https://doi.org/10.1021/acs.jpcb.6b09973.

Vasilescu AM, Vasilescu AG, Sima LE *et al.* A novel cytotoxic anti-B7-H3 affibody with therapeutic potential in acute myeloid leukemia. *Front Pharmacol* 2025;16:1684226. https://doi.org/10.3389/fphar.2025.1684226.

Walensky LD, Bird GH. Hydrocarbon-stapled peptides: Principles, practice, and progress. *J Med Chem* 2014;57:6275–88. https://doi.org/10.1021/jm4011675.

Wang L, Tharp S, Selzer T *et al.* Effects of a distal mutation on active site chemistry. *Biochemistry* 2006;45:1383–92. https://doi.org/10.1021/bi0518242.

Werle M, Bernkop-Schnürch A. Strategies to improve plasma half life time of peptide and protein drugs. *Amino Acids* 2006;30:351–67. https://doi.org/10.1007/s00726-005-0289-3.

Wittrup KD, Thurber GM, Schmidt MM *et al.* Practical theoretic guidance for the design of tumor-targeting agents. *Methods Enzymol* 2012;503:255–68. https://doi.org/10.1016/B978-0-12-396962-0.00010-0.

Wojcik J, Hantschel O, Grebien F *et al.* A potent and highly specific FN3 monobody inhibitor of the Abl SH2 domain. *Nat Struct Mol Biol* 2010;17:519–27. https://doi.org/10.1038/nsmb.1793.

Woldring DR, Holec PV, Stern LA *et al.* A gradient of sitewise diversity promotes evolutionary fitness for binder discovery in a three-helix bundle protein scaffold. *Biochemistry* 2017;56:1656–71. https://doi.org/10.1021/acs.biochem.6b01142.

Woldring DR, Holec PV, Zhou H *et al.* High-throughput ligand discovery reveals a sitewise gradient of diversity in broadly evolved hydrophilic fibronectin domains. *PLoS One* 2015;10:e0138956. https://doi.org/10.1371/journal.pone.0138956.

Yonesaka K, Haratani K, Takamura S *et al.* B7-H3 negatively modulates CTL-mediated cancer immunity. *Clin Cancer Res* 2018;24:2653–64. https://doi.org/10.1158/1078-0432.CCR-17-2852.

Zafar A, Khatoon S, Khan MJ *et al.* Advancements and limitations in traditional anti-cancer therapies: A comprehensive review of surgery, chemotherapy, radiation therapy, and hormonal therapy. *Discov Oncol* 2025;16:607. https://doi.org/10.1007/s12672-025-02198-8.

Zahnd C, Kawe M, Stumpp MT *et al.* Efficient tumor targeting with high-affinity designed ankyrin repeat proteins: Effects of affinity and molecular size. *Cancer Res* 2010;70:1595–605. https://doi.org/10.1158/0008-5472.CAN-09-2724.

Zang X, Sullivan PS, Soslow RA *et al.* Tumor associated endothelial expression of B7-H3 predicts survival in ovarian carcinomas. *Mod Pathol* 2010;23:1104–12. https://doi.org/10.1038/modpathol.2010.95.

Zhang JH, Shan LL, Liang F *et al.* Strategies and considerations for improving recombinant antibody production and quality in Chinese hamster ovary cells. *Front Bioeng Biotechnol* 2022;10:856049. https://doi.org/10.3389/fbioe.2022.856049.

Zhang W, Wang H, Feng N *et al.* Developability assessment at early-stage discovery to enable development of antibody-derived therapeutics. *Antib Ther* 2023;6:13–29. https://doi.org/10.1093/abt/tbac029.

Zhou WT, Jin WL. B7-H3/CD276: An emerging cancer immunotherapy. *Front Immunol* 2021;12:701006. https://doi.org/10.3389/fimmu.2021.701006.

© The Author(s) 2026. Published by Oxford University Press. This is an Open Access article distributed under the terms of the Creative Commons Attribution-NonCommercial License (https://creativecommons.org/licenses/by-nc/4.0/), which permits non-commercial re-use, distribution, and reproduction in any medium, provided the original work is properly cited. For commercial re-use, please contact reprints@oup.com for reprints and translation rights for reprints. All other permissions can be obtained through our RightsLink service via the Permissions link on the article page on our site—for further information please contact journals.permissions@oup.com.
Protein Engineering, Design and Selection, 2026, 1–12
https://doi.org/10.1093/protein/gzag031
Original Article